Eleventh International Conference on Computational Fluid Dynamics (ICCFD11), Maui, HI, USA July 11-15, 2022 **ICCFD11-2022-0201**

Turbulence development assessment in a LES simulation

M. Bove*, G. Cazes*, M. Draper* and M. Mendina*
Corresponding author: mbove@fing.edu.uy

* Facultad de Ingeniería, Universidad de la República,
Julio Herrera y Reissig 565, Montevideo, Uruguay.

Abstract: This proposal aims to analyze conditions that allow the development of turbulence in a LES simulation with uniform velocity and temperature initial and boundary conditions first and with conditions obtained from WRF simulations ultimately. According to recent studies and considering the underlined governing equations of the simulation, a transition zone should occur over which resolved-scale turbulence is generated within the flow. This transition zone is referred to as fetch which consists of the distance into the LES domain from the inflow boundary over which the turbulence motions approaches an equilibrium. Here, we assess the different fetches that arise and the characteristics turbulent motion that develops under different conditions and configurations.

Keywords: CFD, LES, WRF, Turbulence.

1 Introduction

Many science and engineering problems, such as wind energy production, flow over complex terrain, pollutants transport and meteorological prediction of certain clouds, depend on the Planetary Boundary Layer (PBL) [1], which is the portion of the troposphere that is directly influenced by the Earth's surface [2]. Accurate modelling of PBL phenomena requires simultaneous representation of a wide range of scales, from the synoptic and mesoscale to the three-dimensional boundary layer turbulence [3]. Numerical Weather Prediction (NWP) models are extensively used for mesoscale simulations, with domain dimensions ranging from a few hundreds meters to a thousand kilometers. However, the relatively coarse resolution of these models cannot capture the microscale dynamics of the PBL [4].

Since the pioneering work of Deardoff [5, 6] Large Eddy Simulation (LES) has been extensively used to reproduce a variety of PBL regimes and better investigate some atmospheric problems, urban impact on microclimate, and the influence of land-atmosphere exchanges on the transport of pollutants [4]. Due to the expansion of computer capabilities, fine-scale atmospheric models have improved the description of small-scale turbulent motions, making LES models ideal for PBL studies [4, 7].

However, to accurately represent the atmospheric conditions of geographic scales broader than the usual domains of microscale models like LES, it is necessary to couple the LES model with a mesoscale one, such as the Weather Research and Forecasting (WRF) model [8]. This implementation has the known problem on how to develop turbulence in the LES simulation, given that the initial and boundary conditions provided by the mesoscale model do not contain any spectrum of turbulent motion. This happens because WRF and most of the NWP models use a Reynolds Averaged Navier Stokes (RANS) [9] approach, which provides time-averaged fields and does not resolve any turbulent scale explicitly. Therefore, the boundary conditions obtained for the nested LES domain are smooth (i.e. do not contain any turbulence) [3, 10, 11, 12, 13]. As a consequence, long fetches are required for turbulence to emerge. This generates an under-developed transitional state which affects turbulence related magnitudes and modifies the structure of the simulated PBL. This is particularly relevant in the Convective Boundary Layer (CBL), which needs turbulent mixing to develop its whole plethora of phenomena [2, 3]. Even with high resolution ($\sim$ 10 m) in LES domains, a large modeled area is necessary for small scales turbulence to develop [1, 10, 12, 14, 15, 16].

Consequently, this work aims to study under which conditions and with what characteristics turbulence is developed in a LES simulation with boundary conditions that do not contain any turbulence.

This article is organized as follows: in Section 2 a brief summary of the flow solver used to run the simulations is presented. The simulations setups and the grids geometries are described in Section 3. In Section 4 all simulated cases results are presented and discussed. Finally, conclusions are compiled in Section 5.

2 Flow solver

For the LES simulations an open-source, finite volume CFD solver called caffa3d is used [17, 18, 19]. This solver has second order accuracy in space and time, and is used to simulate three-dimensional incompressible flows in block structured curvilinear grids.

The domain is divided in unstructured blocks of structured grids. The same block structure is used for parallelization through MPI [17] by domain decomposition. The mathematical model comprises the mass balance equation (1) and momentum balance equation (2) for a viscous incompressible fluid, together with generic passive scalar transport equation (3) for scalar field ϕ with diffusion coefficient Γ. The balance equations are written for a region Ω, limited by a closed surface S, with outward pointing normal $\hat{n}_s$

$$\int_S (\vec{v} \cdot \hat{n}_s)\, dS = 0 \tag{1}$$

$$\int_\Omega \rho \frac{\partial u}{\partial t} d\Omega + \int_S \rho u\, (\vec{v} \cdot \hat{n}_s)\, dS = \int_\Omega \rho\beta(T - T_{ref})\vec{g} \cdot \hat{e}_1\, d\Omega + \int_S -p\hat{n}_s \cdot \hat{e}_1\, dS + \int_S (2\mu D \cdot \hat{n}_s) \cdot \hat{e}_1\, dS \tag{2}$$

$$\int_\Omega \rho \frac{\partial \phi}{\partial t}\, d\Omega + \int_S \rho\phi\, (\vec{v} \cdot \hat{n}_s)\, dS = \int_S \Gamma\, (\nabla\phi \cdot \hat{n}_s)\, dS \tag{3}$$

where $\vec{v} = (u, v, w)$ is the velocity, ρ is the density, β is the thermal expansion factor, T is the temperature and T_{ref} a reference temperature, $\vec{g}$ is the gravity, p is the pressure, μ is the dynamic viscosity of the fluid and D is the strain tensor.

The generic transport equation (3) for passive scalars can be used to implement other physical models like heat transport and turbulence models, especially used in these simulations. The use of equations in their global balance form, together with the finite volume method, as opposed to the differential form, favors enforcing conservation properties for fundamental magnitudes as mass and momentum into the solving procedure [17, 18, 19].

To handle correctly the linearization and subsequent coupling of linear systems for each equation in the mathematical model, an outer-inner iteration scheme for each time step is used, as shown in Fig. 1. Regarding the subgrid modelling the standard Smagorinsky model with a coefficient of 1.6 was used. [20].

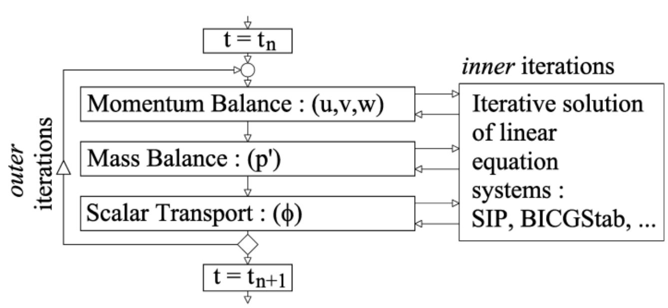

Figure 1: Iteration scheme for one time step. Extracted from [17].

3 Simulation setup

As described in Section 1, the aim of this article is to explore under which conditions turbulence is developed in a LES simulation, with the ultimate goal of recreating a convective PBL. Therefore, different flow conditions are tested, starting with the most basic, and adding more realistic conditions to ultimately receive a temperature profile from a mesoscale simulation using the WRF model.

3.1 Grids

For these simulations two different grids with a simple geometry are implemented. For the simplest case which has a horizontal inflow velocity of 10 m/s without temperature nor heat considerations, a long prismatic grid (Grid A) of $48 \times 1.0 \times 0.5$ km is considered in order to have plenty of space for the turbulence to develop [12, 14]. This grid has uniform horizontal resolution (20 m side square cells) and vertical resolution that expands with height starting at 0.67 m for the first cell. For the other cases where the flow conditions act as a catalyst for the turbulence development, a grid (Grid B) of the following dimensions is considered: $13.86 \times 2.0 \times 1.5$ km. In this configuration, due to the shorter of the domain more space to the sides and above could be obtained for the same computational cost. Having up to 1.5 km in height is useful for the vertical motions to freely move and prevent any constraint that the top of the grid could bring. Thanks to an MPI implementation in caffa3d it is possible to drastically reduce computation time by dividing the domain in multiple regions and resolving the equations for each one of them in separate nodes [17]. For these cases 36 regions are used for both grid configurations, while maintaining the number of finite volumes (cells) to 240000. In Table 1 a summary of the described grid configuration is presented, and in Fig. 2 and Fig. 3 schematic representations of the grid and the grids' regions are shown.

Grid	A	B
Length [km]	48	13.86
Width [m]	1.0	2.0
Height [m]	0.5	1.5
Horizontal resolution (i) [m]	20	20
Horizontal resolution (j) [m]	20	20
First cell height [m]	0.67	1.00
Number of regions	36	36
Total cells	240000	240000

Table 1: Grids configuration.

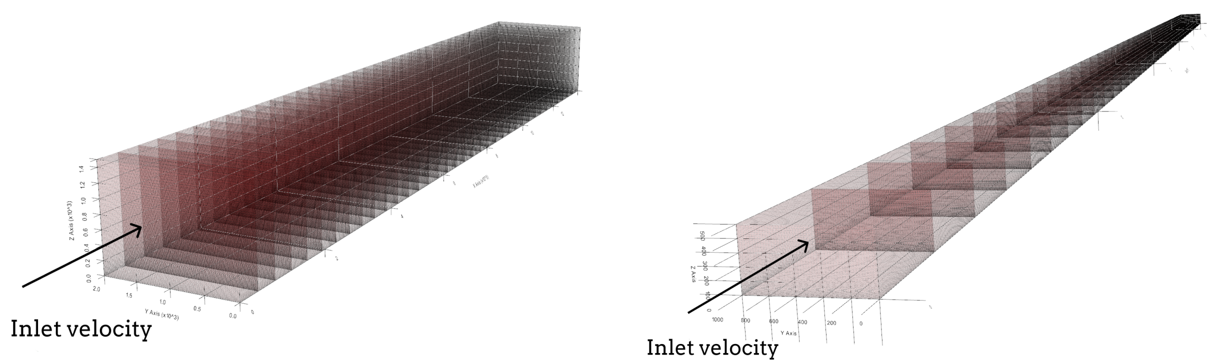

(a) Grid A. Dimensions: $48 \times 1.0 \times 0.5 \times$ km.

(b) Grid B. Dimensions: $13.86 \times 2.0 \times 1.5 \times$ km.

Figure 2: a 3D schematic representation of the the two grids used in the simulations.

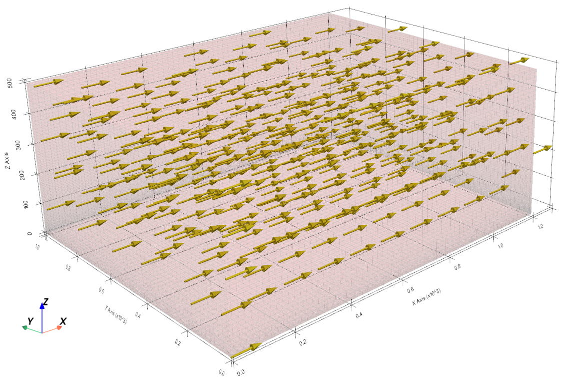

(a) A Grid A region. Dimensions: $1.2 \times 1.0 \times 0.5\,\text{km}$.

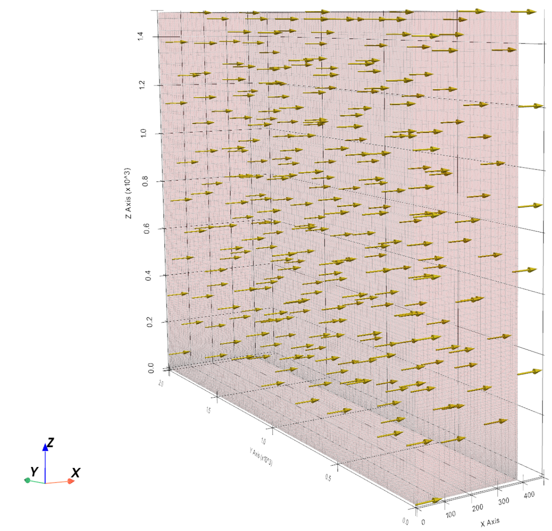

(b) A Grid B region. Dimensions: $0.39 \times 2.0 \times 1.5\,\text{km}$.

Figure 3: a 3D schematic representation of one of the regions that compose the two grids used in the simulations. Both Grid A and Grid B are composed of 36 regions. Yellow arrows indicate the flow direction.

3.2 Cases

Several cases with different flow conditions are tested. First, a simple case with a homogeneous horizontal velocity as inflow with no temperature nor heat consideration is simulated (*hal001*). Second, a temperature perturbation method [11, 21] is implemented in order to accelerate the onset of turbulent motion (*qer001*). Then, a heat flux of about 70 Wm^{-2} is prescribed to the surface in order to induce a buoyancy driven turbulence (*qet001*); a heat flux of 140 Wm^{-2} was also tested, and insights regarding both conditions are commented in Section 5. Given that caffa3d is designed to simulate incompressible flows [17], a new term is added to contemplate the adiabatic expansions and compressions that occur when the air inside a PBL is cooled or heated (*qrf001*). Finally, a more realistic inflow condition is simulated by prescribing a temperature profile obtained from a WRF simulation to the inlet boundary condition (*qrg001*).

Case	Grid	Pert. method	Ad. exp.	Inflow condition		Surface heat flux [Wm^{-2}]
				U [ms^{-1}]	T [K]	
hal001	A	No	No	10	273	0
qer001	B	Temperature	No	10	292	0
qet001	B	No	No	10	292	70
qrf001	B	No	Yes	10	292	70
qrg001	B	No	Yes	10	WRF profile	70

Table 2: Simulated cases, its flow conditions and features.

Table 2 presents and defines all simulated cases. A more detailed explanation on each case configuration is presented below. A discussion about the results of each of these simulations is developed in Section 4.

3.2.1 hal001

Most simple case with just a uniform inflow velocity of 10 ms^{-1} with no temperature or heat considerations. It uses Grid A (see Table 1 and Table 2).

3.2.2 qer001

The Stochastic Perturbation Method proposed by Muñoz-Esparza [11, 22] was implemented in order to accelerate the onset of turbulent motion (i.e. reduce the required fetch). This method, which has been used by several authors [1, 3, 14, 22, 23, 24] consists in rectangular patches of uncorrelated, stochastically generated perturbations applied the potential temperature field along three consecutive strips extending into the domain from the inflow plane.

Random perturbations of amplitude $\Delta\theta$ are introduced in each perturbation zone. Said amplitude is modelled as a random variable with a symmetric uniform distribution.

$$\theta_{pert} = \theta + \Delta\theta \tag{4}$$

Perturbations are ordered by cells. A cell is a horizontal set of 8×8 points on the grid. All the grid's points that belongs to the same cell have the same perturbation $\Delta\theta$ at a certain simulation time step. Cells are adjacent to the domain's boundaries, in particular it must be adjacent to the inflow boundary. Fig. 4 shows schematic views of the perturbation cells in relation to the simulated domain.

Patches of correct sizes and amplitudes should produce buoyant instabilities that rapidly amplify via the nonlinear dynamics of the governing flow equations, generating turbulence that is consistent with the forcing [24].

The authors of the method analyzed the optimal amplitude for the perturbations as a function of the Eckert number:

$$E_c = \frac{U_g^2}{c_p \, \Delta\theta_{max}} \tag{5}$$

where U_g corresponds to the geostrophic wind. They came to the conclusion that the optimum is achieved for $E_c \approx 0.2$.

The frequency of the perturbations is also discussed and expressed in terms of the following dimensionless number:

$$\Gamma = \frac{t_p U_1}{d_c} \tag{6}$$

where t_p is the period of the perturbations, U_1 is the value of the inflow velocity in the first point from the ground, and d_c corresponds to the diagonal of a cell.

Furthermore, as recommended in [14, 24] the SCPM-T method is applied from the floor to up to two thirds of the PBL height.

(a)

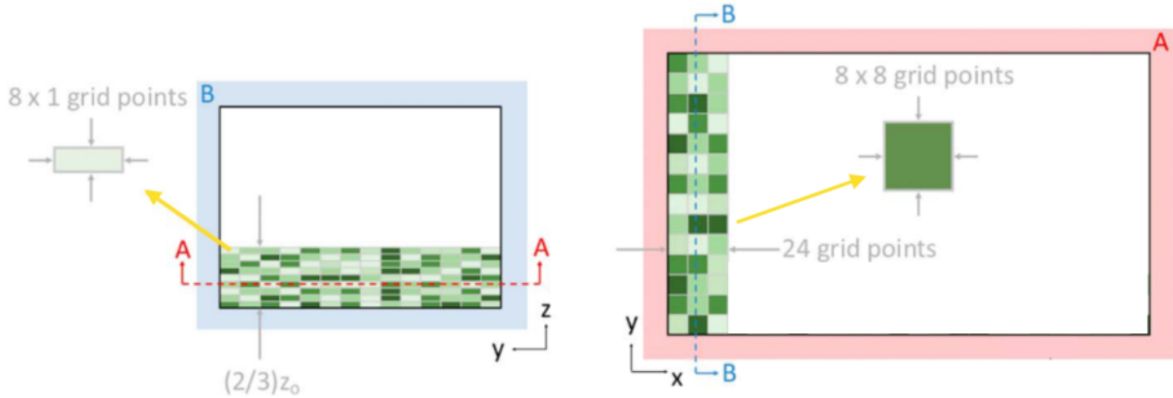

(b)

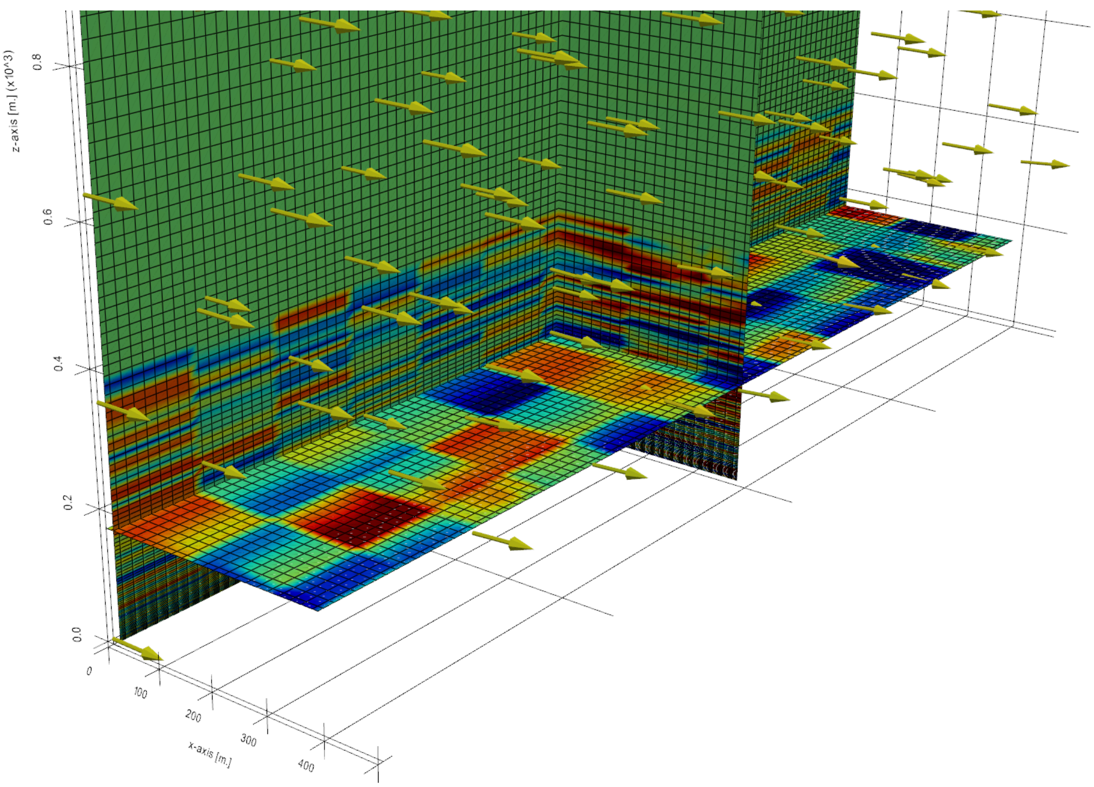

Figure 4: (a) Schematic domain adapted from [14] and (b) actual simulated domain (its first 600 m) showing cross Sections in the horizontal and vertical planes along which the stochastic cell perturbations are applied. z_o corresponds to the PBL height. (b) Also indicates the flow direction by showing the velocity vector as yellow arrows.

3.2.3 qet001

A uniform surface heat flux of 70 W/m^2 is added to this case in order to evaluate the effects of a buoyancy driven turbulence generation. It uses Grid B (see Section 1).

3.2.4 qrf001

In this case that also uses Grid B, besides the surface heat flux, a modification to caffa3d flow solver source code was done in order to model the adiabatic expansions and compressions that occur in a compressible flow exposed to changes in temperature, like air in the atmosphere.

In a CBL, vertical vortices associated with the ascent of hot air and descent of cold air are developed. The air parcels in these vortices experiments adiabatic expansions and compressions when ascending and descending, respectively. This cooling and heating increases and decreases the density of air parcels, which stabilizes the effect of the buoyancy and limits the height of the eddies. [2]

As caffa3d is designed to simulate incompressible flows, it cannot recreate the previously described physical phenomenon without some modification on its source code. That is because the energy balance equation does not contain a term associated with compression mechanical work. It is therefore proposed, to incorporate the thermal effects of compression mechanical work in a explicit way into caffa3d source code. Starting off with the First Law of Thermodynamics:

$$c_p \frac{dT}{dt} = \dot{q} + \nu \frac{dP}{dt} \tag{7}$$

where c_p is the specific heat capacity at constant pressure, T is the temperature, $\dot{q}$ the thermal power supplied to the fluid and P is the pressure. The term on the left represents the total differential of the sensible enthalpy, the first term on the right accounts for the thermal power supplied to the fluid, and the second one is the compression mechanical work. This last term is the one that caffa3d lacks and will be explicitly modelled.

Approximating the pressure field by an hydostatic distribution and differentiating in time, the following expression is obtained:

$$\frac{dP}{dt} \approx -\rho g U_z \tag{8}$$

where U_z is the vertical component of the velocity field.

Hence, the main thermal effects associated with adiabatic expansions and compressions due to the ascent or descent of air parcels can be represented in caffa3d by adding this term to the right side of Equation 3.

This implementation was tested in the coupling presented in this work. Results show that eddies are constrained in height as appreciated in Fig. 5.

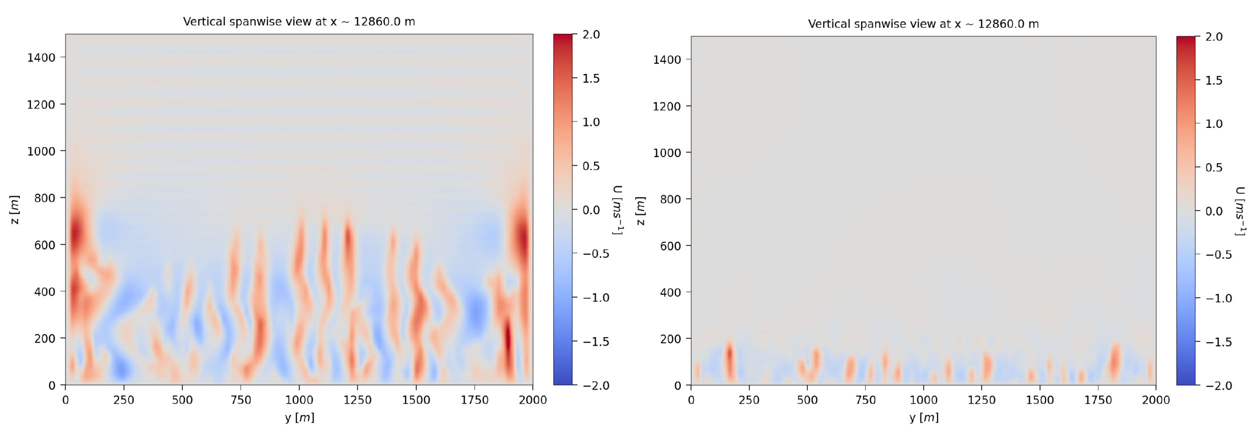

(a) (b)

Figure 5: Spanwise slices of the vertical velocity component at a position 12.86 km from the inflow for a LES simulation with uniform velocity and temperature profiles (a) without the term that takes adiabatic expansion and compressions into account and (b) with the term.

3.2.5 qrg001

In this simulation, besides the surface heat flux and the modification to contemplate adiabatic expansions and compressions, a temperature profile obtained from a WRF simulation is added at the inflow. Grid B is utilized in this case too.

A sample day where the temperature profiles present a capping inversion was chosen to be simulated. From this WRF simulation ran at a local time of 10, 11 and 12 A.M. (UY, GMT-3) it can be seen that a convective PBL is developed in the morning with its characteristic capping inversion and then it starts to disappear as the rising sun heats the air around the surface [**?**]. Fig. 6 shows the absolute and potential temperature, and the dry static energy over specific heat profiles of the WRF simulation.

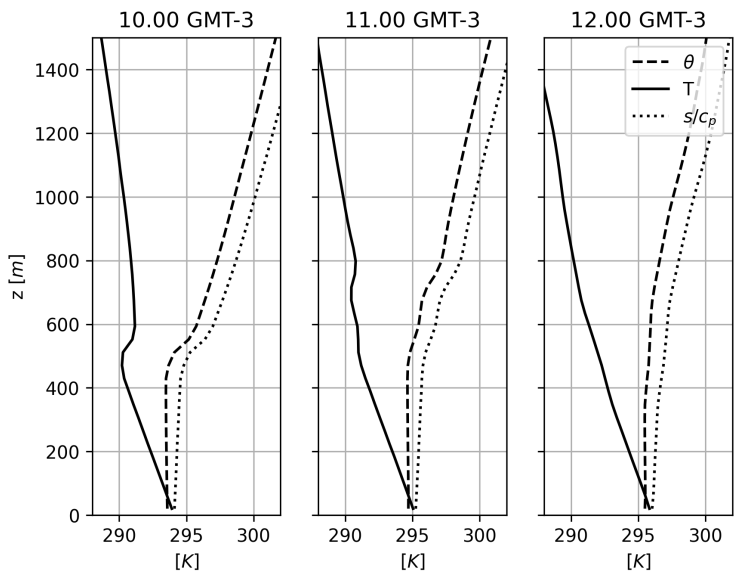

Figure 6: Absolute and potential temperature and dry static energy divided by specific heat profiles of a WRF simulation of a morning with a convective PBL. The 10 A.M profile is prescribed in the LES simulation of case *qrg001*.

In order to prescribe this temperature condition to the LES simulation as an inflow boundary condition, an interpolation of the WRF points was made to fit the profile to Grid B. Then, the interpolated profile was copied along the spanwise direction and incorporated as caffa3d simulation boundary conditions. In Fig. 7a the WRF points and the interpolated ones are shown, and Fig. 7b shows a spanwise vertical plane of the temperature field at a position 1 m from the inflow of *qrg001* simulation in order to show that the capping inversion is present at the entrance of the domain.

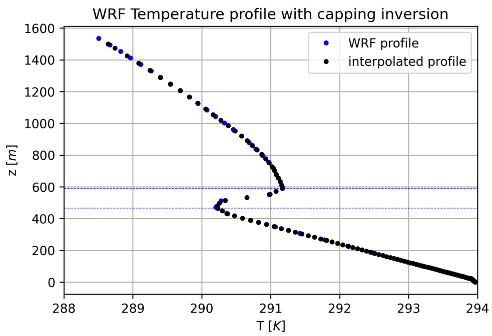

(a)

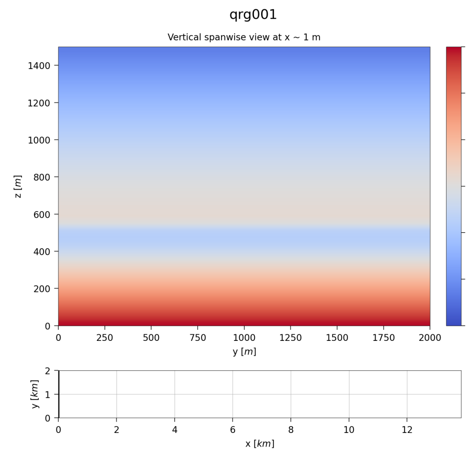

(b)

Figure 7: (a) Temperature profile of a PBL with capping inversion obtained from a WRF simulation, and (b) a spanwise view of the inflow temperature field for case *qrg001* showing the capping inversion as a stripe around 500 m.

4 Results discussion

4.1 hal001

In this simple case, with just an homogeneous uniform inflow velocity, some turbulent motion starts to appear at about 15 km from the inflow, and it reaches a maximum at about 25 km. This can be seen in Fig. 8 which is a horizontal view of the vertical component of the velocity and specially in Fig. 9b which shows the evolution of Turbulent Kinetic Energy (TKE) over the streamwise direction. In Fig. 11 the increase in amplitude for all velocity components (specially for the vertical one) as the distance to the inflow is increased can be appreciated. In the same way, in Fig. 10 a tendency for a more evenly distributed vertical motion can be noticed as the slice moves away from the inflow.

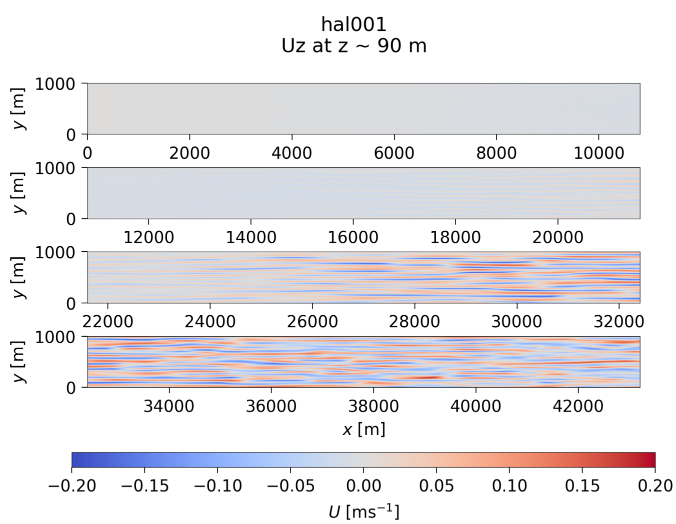

Figure 8: Instantaneous vertical velocity at a horizontal plane 90 m above the terrain for the simplest case *hal001*. Each subplot represents a portion of the domain in the along the x axis. The velocity was sampled after 6 h of simulation.

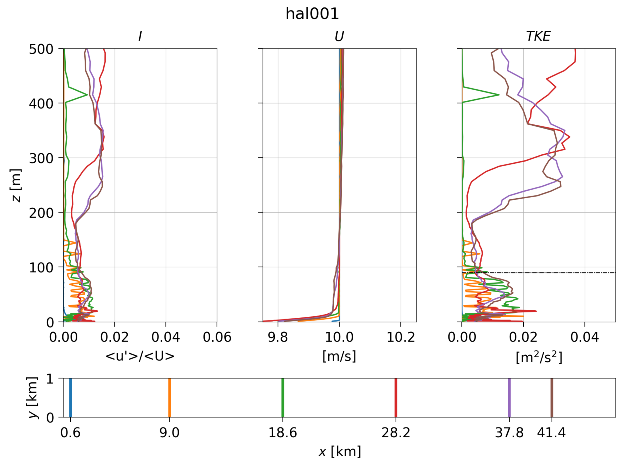

(a)

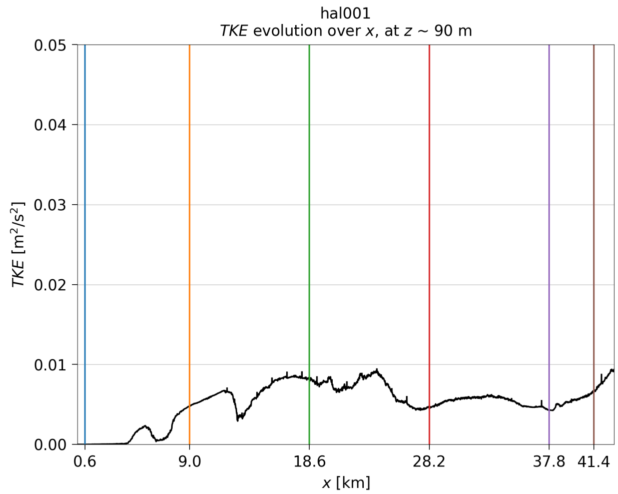

(b)

Figure 9: (a) From left to right on each subplot: Turbulence Intensity (I), Mean Velocity $< U >$, and Turbulent Kinetic Energy (TKE). (b) Evolution of TKE over fetch (along the x axis). TKE was temporally averaged in a 3 h window and spatially in the y axis.

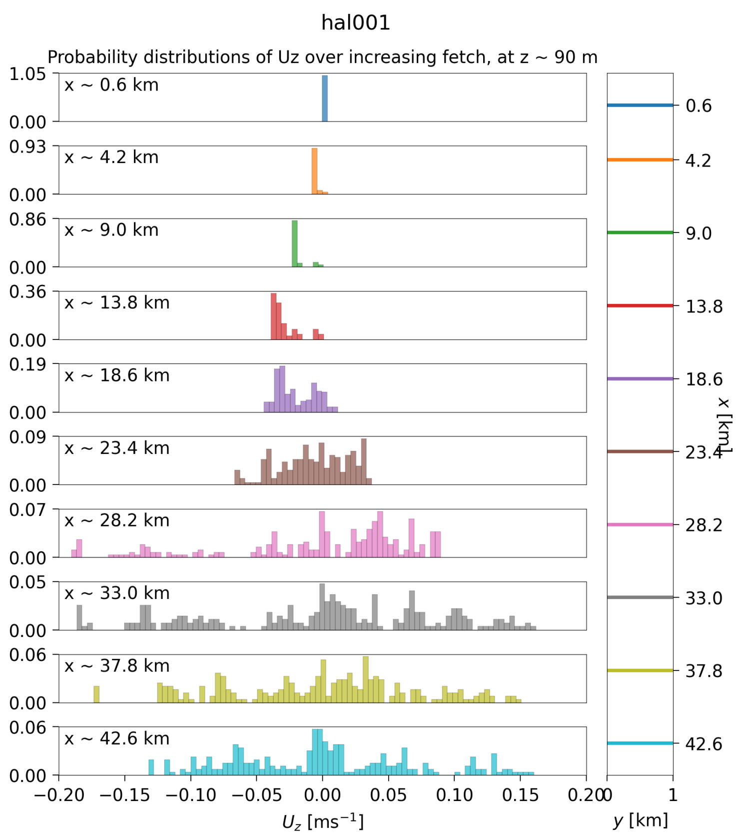

Figure 10: Vertical velocity component (U_z) probability distribution along different transversal slices. Each subplot corresponds to a slice in a different position along the domain. The subplot at the left is a schematic representation of the domain seen from above. The velocity was averaged in a 3 h window and taken along the spanwise center of the domain.

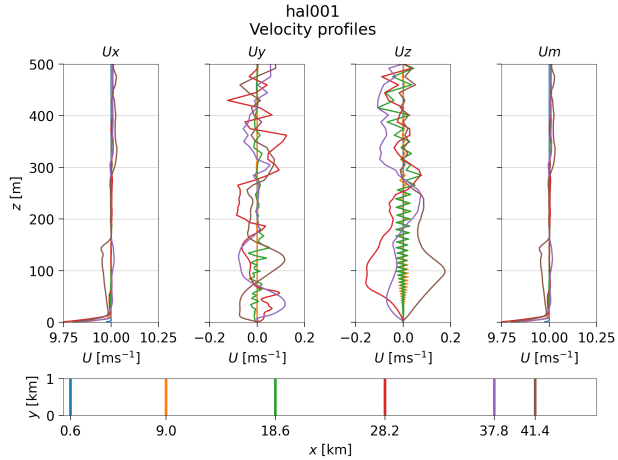

(a)

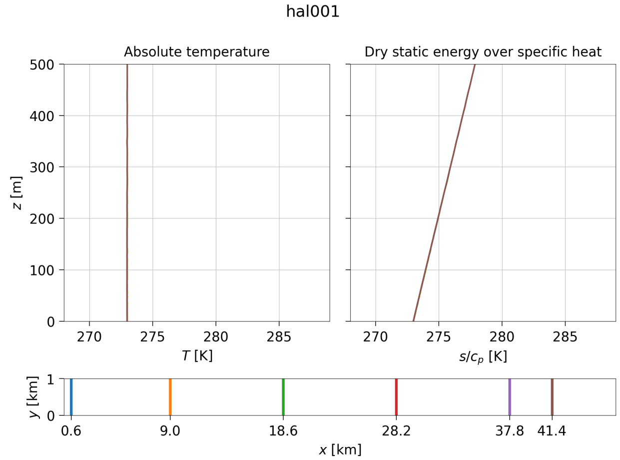

(b)

Figure 11: (a) Velocity profiles, from left to right: Ux, Uy, Uz and Um the velocity module. (b) Absolute temperature and dry static energy over specific heat profiles. The color of the lines correspond to a certain position along the x axis as seen in the subplot at the bottom which represents the domain seen from above. These are instantaneous profiles after 6 h of simulation.

4.2 qer001

As described in Section 3.2.2, the SCPM method applied to the temperature field is tested. In Fig. 12 instantaneous vertical velocity component contours show the rapid onset of turbulent motions due to the perturbations in the temperature field, which are clearly appreciated in Fig. 15b having around 2 K of amplitude. In the aforementioned slices, it is noteworthy the increase in height of the eddies, that reach the top of the grid at around 8 km. Turbulence motion, reaches a maximum at about 2 km judging not only the Uz amplitude in Fig. 12, but the various turbulence metrics depicted in Fig. 13a, specially the TKE that has its maximum around 2 km as shown in Fig. 13b. Then, as the effects of the perturbations diminish along the domain, so does the TKE. Another way to see the same behaviour is provided by Fig. 14 which shows the Uz probability distributions along different transversal slices, the more evenly distributed the vertical velocity components are, the greater the turbulence. These observations are consistent with other work in the matter [11, 14].

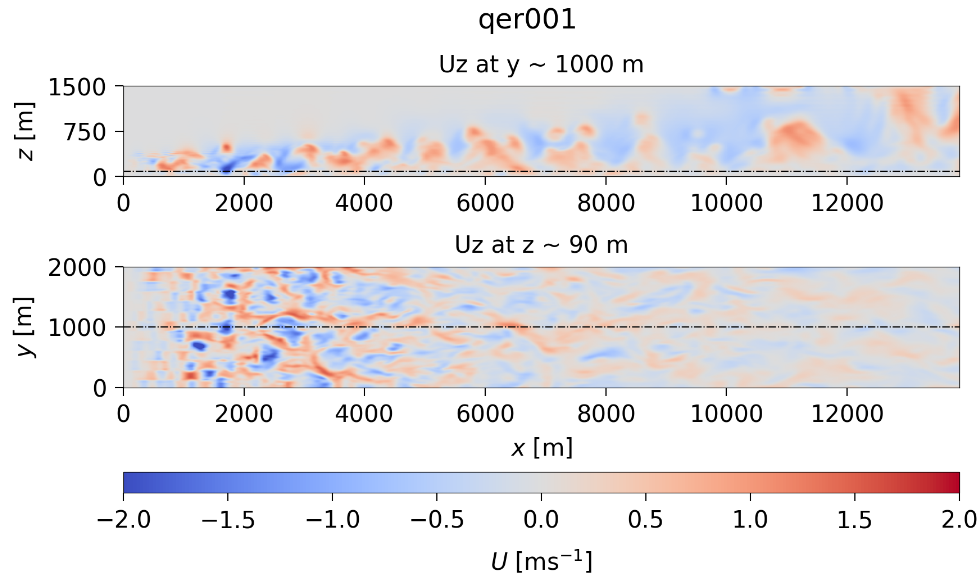

Figure 12: Streamwise (top) and horizontal (bottom) views of contours of instantaneous vertical velocity component (Uz) at $y \sim 1000\,\text{m}$ and $z \sim 90\,\text{m}$, respectively. The velocity was sampled afeter 6 h of simulation.

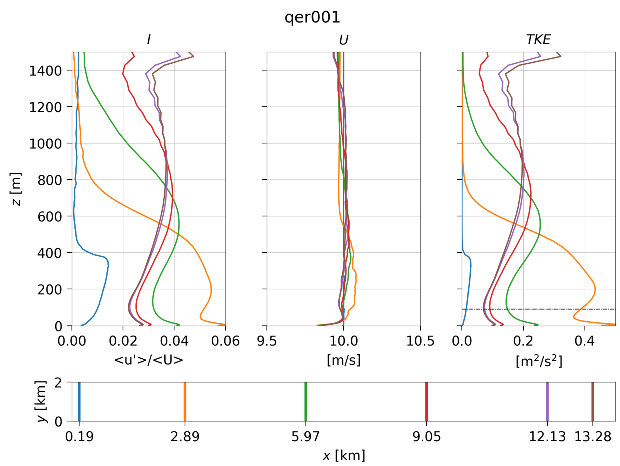

(a)

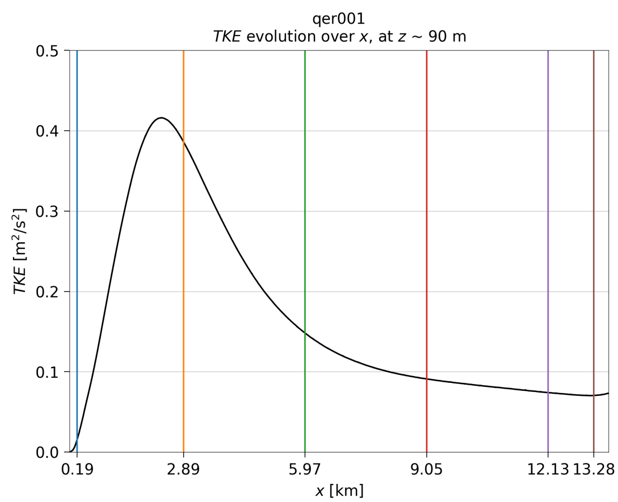

(b)

Figure 13: Turbulent metrics and TKE evolution over fetch, analog to Fig. 9.

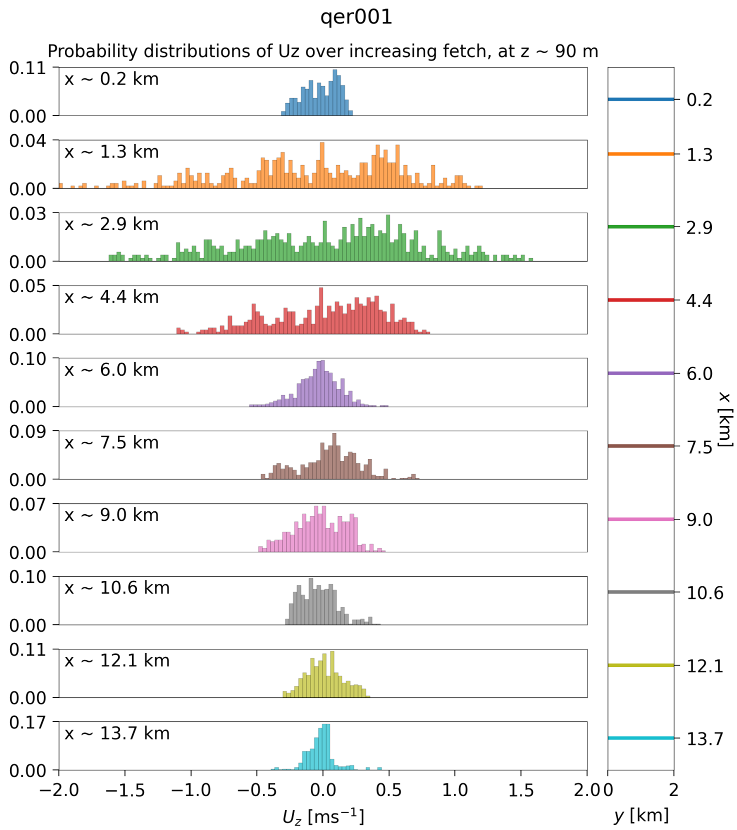

Figure 14: Vertical velocity component (U_z) probability distribution analog to Fig. 10.

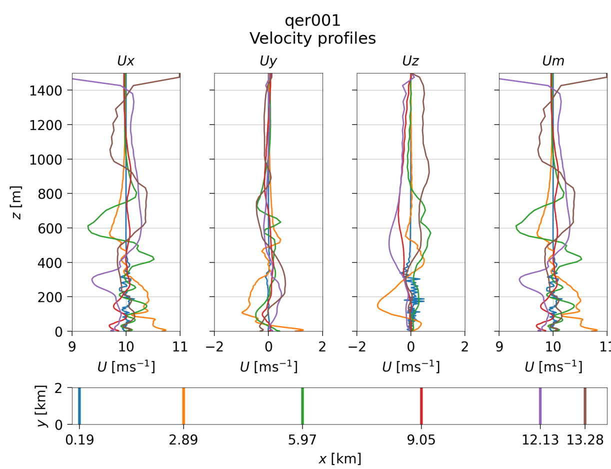

(a) Velocity profiles.

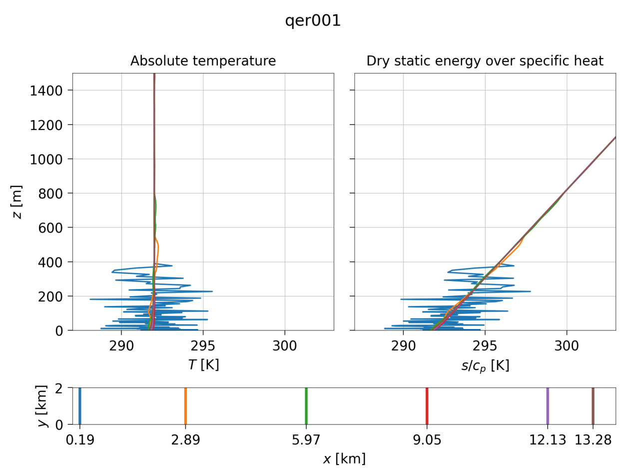

(b) Temperature profiles.

Figure 15: (a) Velocity profiles and (b) absolute temperature and dry static energy over specific heat profiles analog to Fig. 11. The noisy blue line in the temperature and dry static energy profiles show the perturbations applied to the potential temperature field.

4.3 qet001

In this other case, a surface heat flux of about 70 W/m^2 is added to induce a buoyancy driven turbulence [25]. As expected [26, 24, 23], the heat flux accelerates the development of turbulent motion and decrease the fetch considerably, starting to have turbulence at about 7 km (Fig. 16 and Fig. 17b).

Fig. 19 shows the velocity profiles. In contrast with the case *hal001* it can be noticed that the turbulent motions are greatly increased having and amplitude of almost 2 ms^{-1} for the vertical velocity component. Besides, due to the buoyancy driven turbulence that comes from the ground, the turbulent motions are mostly limited to the lower 600 m portion of the domain (Fig. 19b and Fig. 17a). Furthermore, the distribution of vertical motions at a height of about 90 m is similar to that other case as it can be seen in Fig. 18

In the following Figure (Fig. 17) some metrics to evaluate the turbulence are shown. It can be seen how the turbulence intensity and the Turbulent Kinetic Energy (TKE) are all greatest just above the surface and start to decrease in a kind of linear way, to finally go to zero at about 800 m.

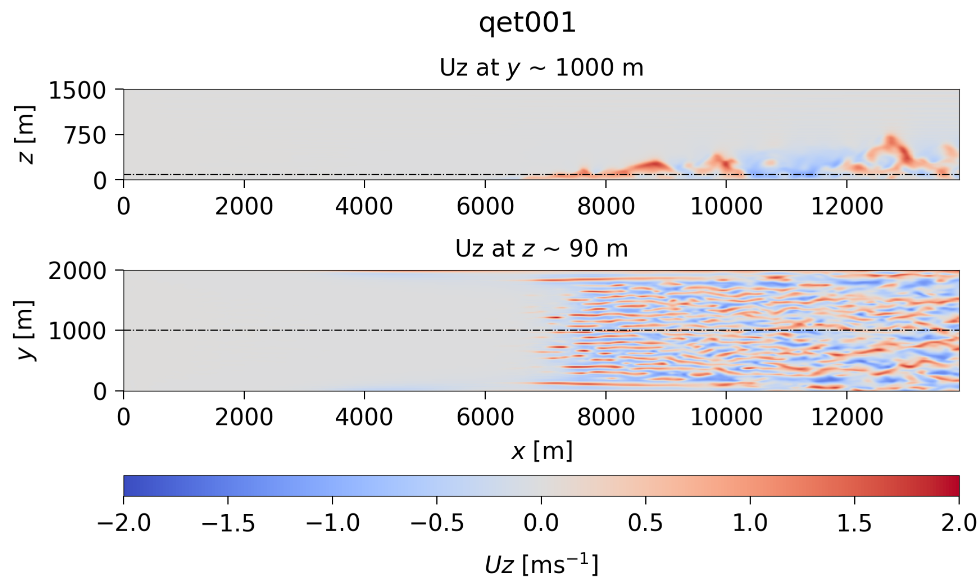

Figure 16: Streamwise (top) and horizontal (bottom) views of contours of instantaneous vertical velocity component (Uz) at $y \sim 1000\,\mathrm{m}$ and $z \sim 90\,\mathrm{m}$, respectively.

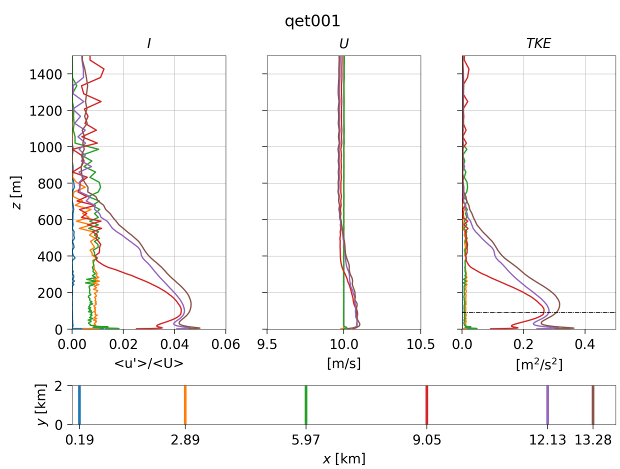

(a) Turbulence metrics.

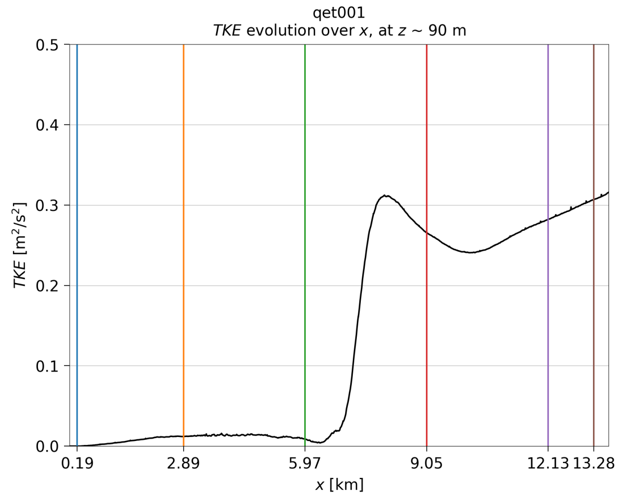

(b) Evolution of TKE over fetch at $z \approx 90m$.

Figure 17: Turbulent metrics and TKE evolution over fetch, analog to Fig. 9.

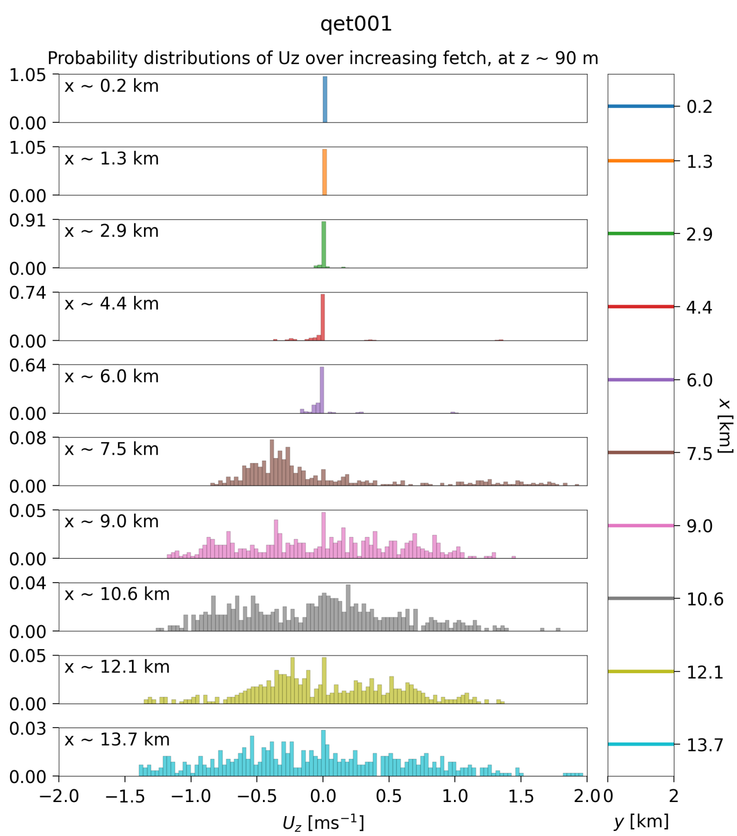

Figure 18: Vertical velocity component U_z probability distribution analog to Fig. 10.

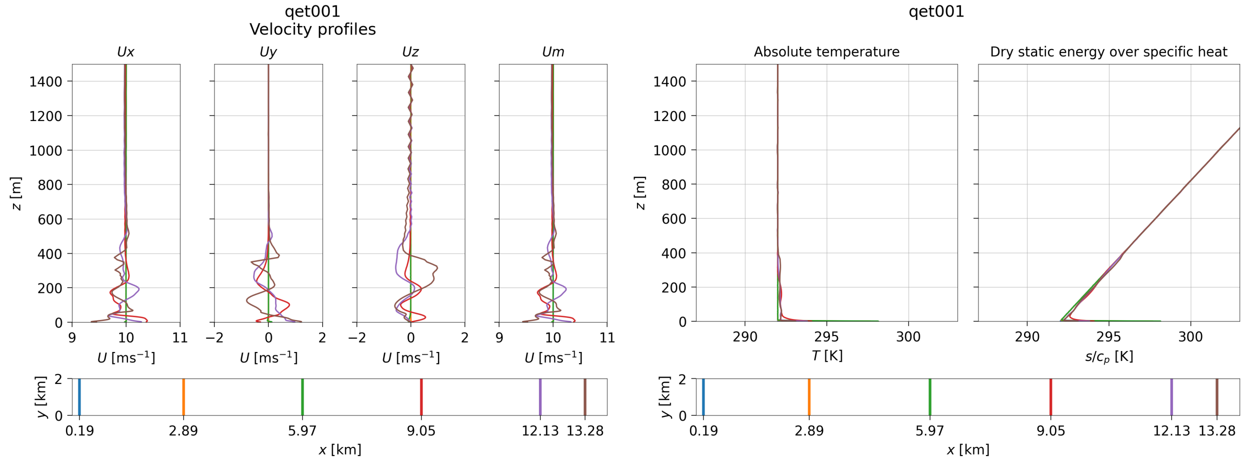

(a) Velocity profiles.

(b) Temperature profiles.

Figure 19: (a) Velocity profiles and (b) absolute temperature and dry static energy over specific heat profiles analog to Fig. 11.

4.4 qrf001

For this case a modification in the caffa3d source code was implemented as explained in 3.2.4. In Fig. 20 a comparison between the simulation without this term (case *qet001*) and with this added term is shown. It can be notice in these spanwise contours of the velocity vertical component that the eddies height are limited due to the adiabatic expansions [2]. In the previous case *qet001* these vortices reached a height of about 800 m, and with the new term, the vortices are limited up to 200 m. It can be appreciated in all the metrics, a decrease in amplitude for all velocity components due to the added term associated with the compression mechanical work.

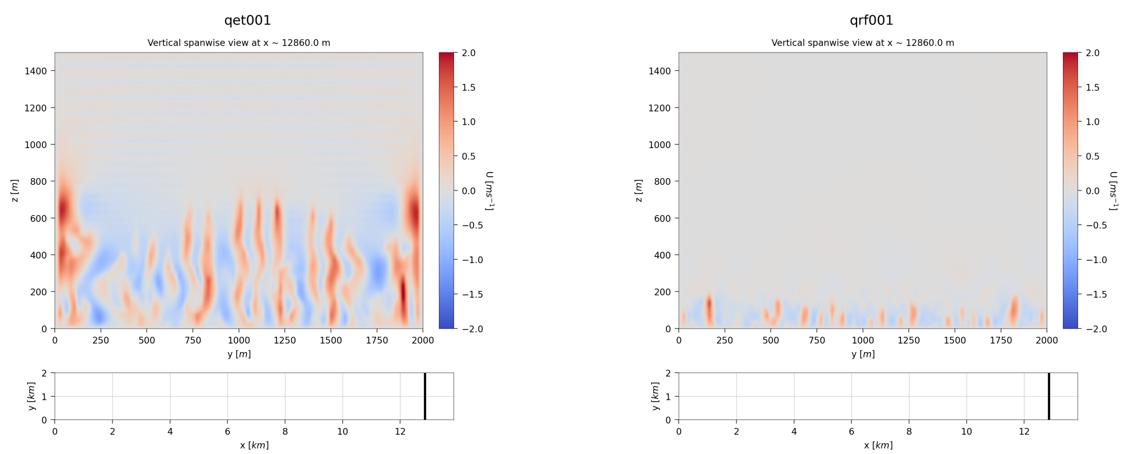

Figure 20: Spanwise slices at 12.86 km from the inflow of the velocity vertical component. Simulation without (left) and with (right) the term associated with compression mechanical work. It is clear how the added term that takes into account the adiabatic expansions and compressions limits the vortices heights from 800 m to 200 m.

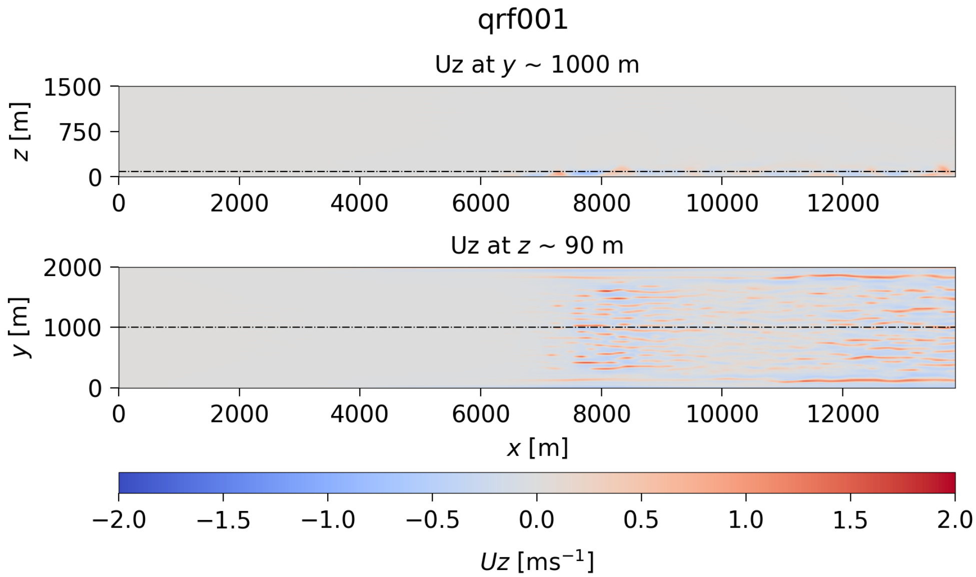

Figure 21: Streamwise (top) and horizontal (bottom) views of contours of instantaneous vertical velocity component (Uz) at $y \sim 1000\,\mathrm{m}$ and $z \sim 90\,\mathrm{m}$, respectively.

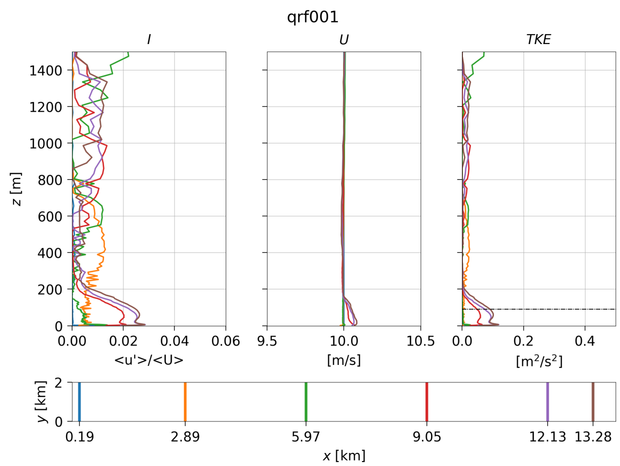

(a) Turbulence metrics.

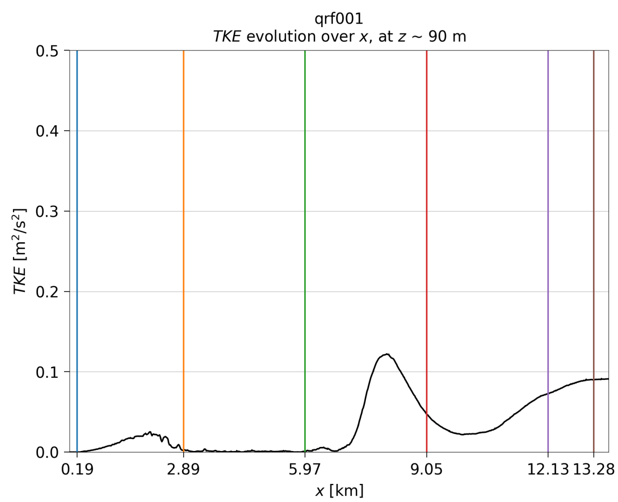

(b) Evolution of TKE over fetch at $z \approx 90m$.

Figure 22: Turbulent metrics and TKE evolution over fetch, analog to Fig. 9.

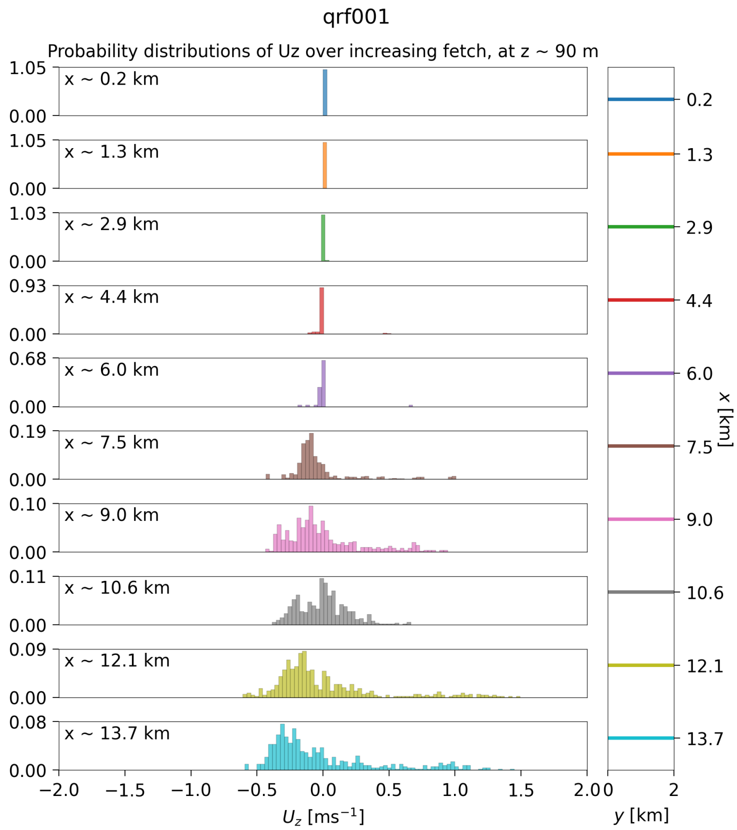

Figure 23: Vertical velocity component U_z probability distribution analog to Fig. 14.

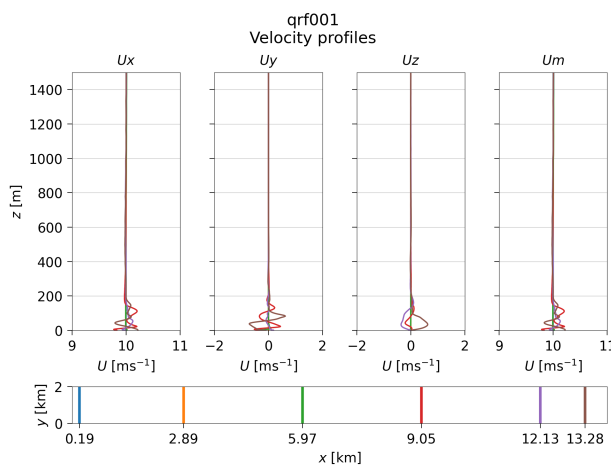

(a) Velocity profiles.

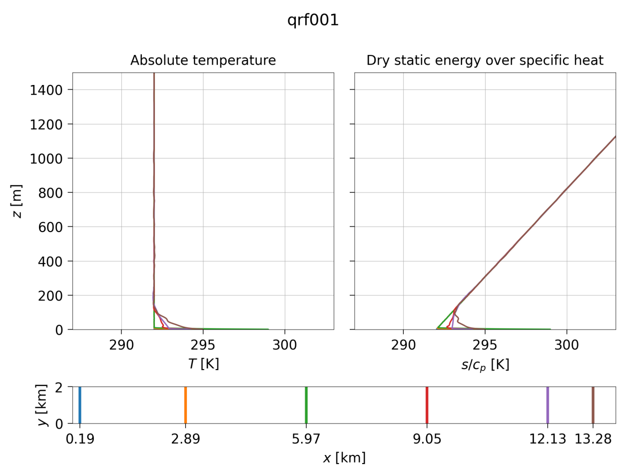

(b) Temperature profiles.

Figure 24: (a) Velocity profiles and (b) absolute temperature and dry static energy over specific heat profiles analog to Fig. 11.

4.5 qrg001

As Fig. 7b shows, the prescribed WRF temperature profile inflow condition maintains its general shape including the capping inversion between 400 and 600 m, that is due to the incorporation of the effects of adiabatic expansions and compressions in the simulated low atmosphere as described in the Section 3.2.4.

In comparison to the previous case *qrf001*, the prescription of the temperature profile acts as a catalyst for the turbulent motion as it has a negative slope (below the capping inversion) that contributes to the buoyancy effects that the surface heat flux already generates. This can be seen in all velocity related figures in some way, but in particular Fig. 27 shows how the probability of Uz values is much more evenly distributed in this case rather than case *qrf001* (Fig. 23).

In Fig. 26b, it can be appreciated how the peak of turbulence (symbolized as a peak in the TKE) is reached at exactly 8 km, and then decreases to ultimately achieve a plateau where it can be assumed that the fetch is over; that is at $x \sim 10.5$ km. Furthermore, it is interesting to notice how the turbulence is trapped inside the capping inversion that starts at $z \sim 400\,\mathrm{m}$ up to 600 m, by seeing all turbulence related metrics in Fig. 26a, and also in the velocity profiles of Fig. 28a.

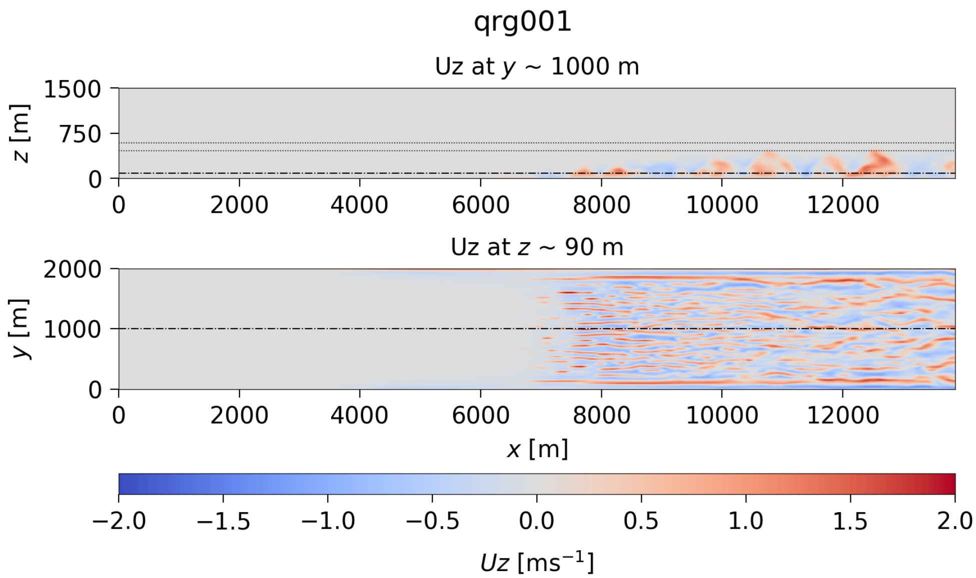

Figure 25: Streamwise (top) and horizontal (bottom) views of contours of instantaneous vertical velocity component (Uz) at $y \sim 1000\,\mathrm{m}$ and $z \sim 90\,\mathrm{m}$, respectively. The capping inversion of the prescribed temperature profile is indicated in a blue dashed line (top subplot).

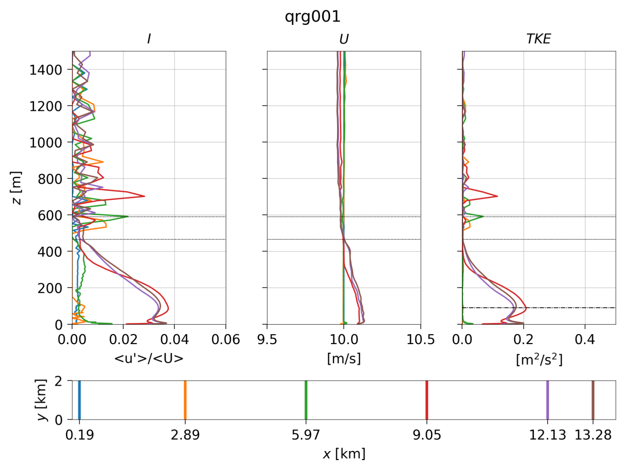

(a) Turbulence metrics.

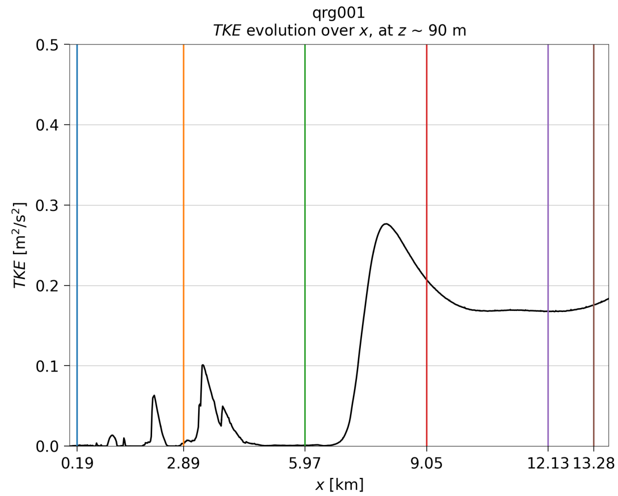

(b) Evolution of TKE over fetch at $z \approx 90m$.

Figure 26: Turbulent metrics and TKE evolution over fetch, analog to Fig. 9.

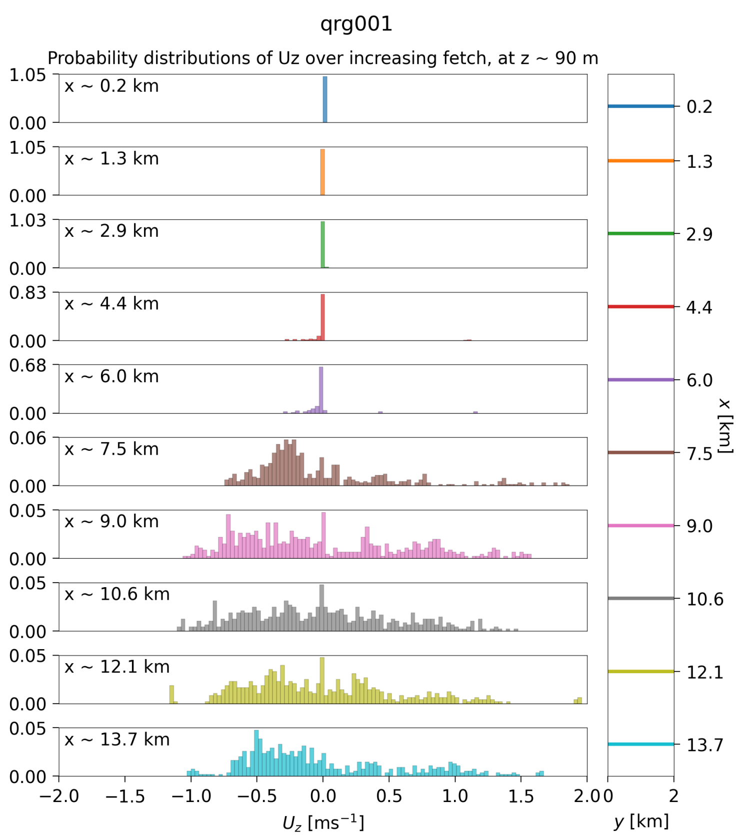

Figure 27: Vertical velocity component U_z probability distribution analog to Fig. 14.

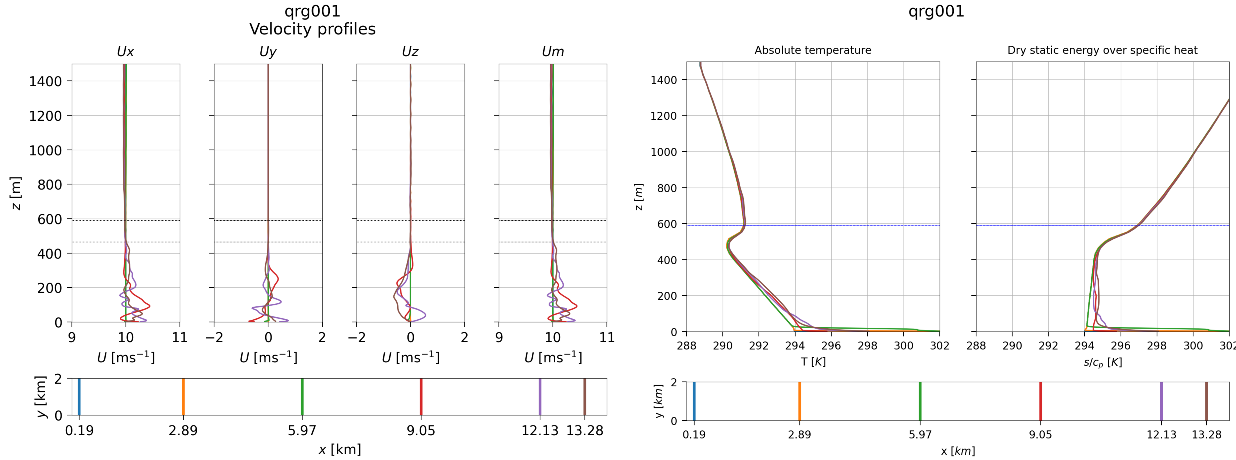

(a) Velocity profiles. (b) Temperature profiles.

Figure 28: (a) Velocity profiles and (b) absolute temperature and dry static energy over specific heat profiles analog to Fig. 11. The capping inversion is indicated in a blue dashed line.

5 Conclusions and future work

These preliminar results pending validation show that turbulence can be developed in a LES simulation when a long enough fetch is considered. Five cases with different setups and flow conditions with growing realism were simulated, their turbulence generation, velocity and temperature characteristics were assessed and its results shown. Starting with a simple case without heat considerations it shows that small turbulence motions are generated if a long fetch of at least 20 km is considered. Then, a temperature perturbation method was tested to show that the fetch could be reduced significantly. However, this method was discarded due to some implementation issue that we could not resolve yet. The incorporation of the compression mechanical work term in the heat equation of the in-house numerical model caffa3d enabled to reproduce the physical phenomenon specially relevant to the PBL of adiabatic expansions and compressions (case *qrf001*). In the last case a prescription of a WRF temperature profile of a morning with a convective PBL with a capping inversion (case *qrg001*) was conducted. This last case sets the stage for the work of coupling a mesoscale model like WRF with a microscale one like caffa3d with the goal of modelling the PBL using realistic meteorological conditions.

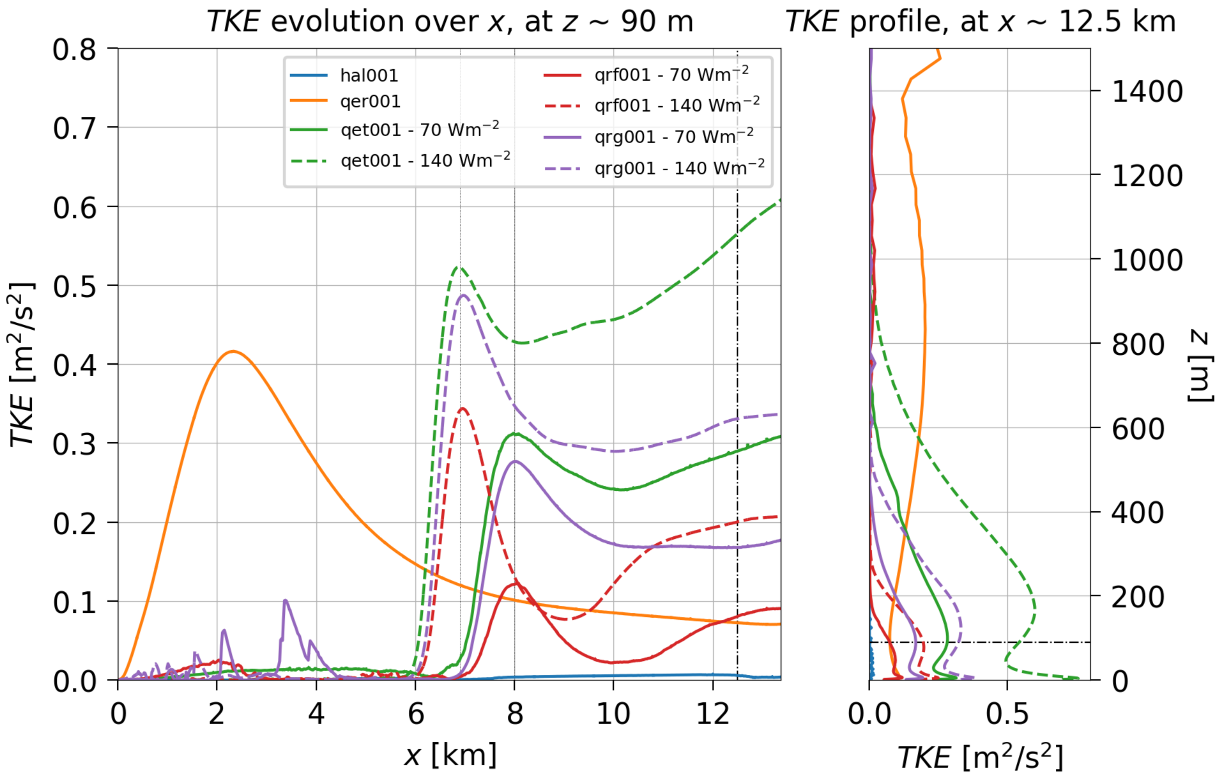

Figure 29: Evolution of Turbulent Kinetic Energy (TKE) along the streamwise axis in the left subplot at $z \sim 90$ m, and TKE vertical profile at $x \sim 12.5$ km in the right subplot. Solid and dashed lines with the same color correspond to the same case with different surface heat flux. Notice how the beginning of the turbulent regime is strictly associated with the magnitude of the imposed heat flux. TKE was averaged in a 3 h window and taken along the spanwise center of the domain.

As a conclusion for the goal of determining the turbulence development and the fetch of these simulations, Fig. 29 depicts the evolution of the TKE along the streamwise x direction at $z \sim 90$ m in the left subplot, and the TKE vertical profile at $x \sim 12$ km for all simulated cases. For cases *qet001*, *qrf001* and *qrg001* it is interesting to notice how abrupt the onset of turbulent motion is at about 7 km due to the instabilities that the surface heat flux generates no longer can be tolerated without a change in the kinematics of the flow. The maximum value in TKE is reached at the same position for all cases exactly at 8 km from the inflow. The solid and dashed lines of the same color depicts the same case with different surface heat flux, and indicates how the sudden leap of turbulence depends on that heat flux and not in the temperature profile, given that the cases with dashed lines (140 Wm^{-2}) have that pronounce liberation of turbulent energy earlier in the domain that the ones with solid lines (70 Wm^{-2}). This TKE curve is similar to the ones found in similar works [1, 22].

This initial abrupt leap in TKE is rapidly subsided having a local minimum at about 10 km and then starting to increase again until it reaches a steady state for cases *qrf001* and *qrg001*. For case *qet001* which has no constraint to the increase in buoyancy driven turbulence the TKE appears to keep increasing as it advances in the domain. Case *qer001* produces greater and earlier TKE due to the perturbation method applied. By looking at the TKE profile at the left of Fig. 29, for case *qer001*, because of the absence of a surface heat flux (or any ground turbulence catalyst for that matter) and being the temperature perturbations the origin for the its turbulence, the TKE profile exhibits a more symmetrical behaviour, having its maximum value at the vertical center of the domain ($z \approx 750m$). In contrast, the other cases have their maximum near the ground at about 80 m as they all have a buoyancy driven turbulence that originates near the ground; although the surface heat flux is not large enough for its effects to subsist above 600 m.

It stands out that the purpose of this work, namely to assess if and when turbulence is generated in a

LES simulation, was accomplished and sets the stage for a coupling of caffa3d in-house LES flow solver with WRF mesoscale model, while augmenting the capabilities of caffa3d flow solver enabling it to resolve some atmospheric processes that occur in the PBL.

For future work a deeper study of the generated turbulence characteristics could be performed. Some metrics like kurtosis, skewness and the energy spectra can be analyzed to augment these evaluations along with a study of the turbulence structures that appears under the different conditions. Although the stochastic cell perturbation method applied to the potential temperature field is the one that has undergone the most development and validation in similar PBL flow simulations [24], some other methods could be tested to check whether they could perform better under certain conditions. For instance, the said stochastic cell perturbation method could be apply to the velocity field [11]. Other perturbations methods like synthetic inflow turbulence methods, for which a correlated turbulence field is applied directly at the inflow planes [24, 27] could be tested too.

6 Acknowledgments

Thanks are due to the National Agency for Research and Innovation (ANII), Uruguay for financing the project NEFELE: *predicción de Nubes para la generación de Energía Fotovoltaica Ensamblando modelación LES y de mEsoescala* (*NEFELE: cloud prediction for photovoltaic energy ensambling LES and mesoscale modelling*) that allowed the development of the work presented in this paper.

References

[1] Laura J Mazzaro, Domingo Muñoz-Esparza, Julie K Lundquist, and Rodman R Linn. Nested mesoscale-to-LES modeling of the atmospheric boundary layer in the presence of under-resolved convective structures. *Journal of Advances in Modeling Earth Systems*, 9(4):1795–1810, 2017.

[2] Roland B Stull. *An introduction to boundary layer meteorology*, volume 13. Springer Science & Business Media, 1988.

[3] Domingo Muñoz-Esparza, Julie K Lundquist, Jeremy A Sauer, Branko Kosović, and Rodman R Linn. Coupled mesoscale-LES modeling of a diurnal cycle during the CWEX-13 field campaign: From weather to boundary-layer eddies. *Journal of Advances in Modeling Earth Systems*, 9(3):1572–1594, 2017.

[4] GC Cuchiara and B Rappenglück. Performance analysis of WRF and LES in describing the evolution and structure of the planetary boundary layer. *Environmental Fluid Mechanics*, 18(5):1257–1273, 2018.

[5] James W Deardorff. Numerical investigation of neutral and unstable planetary boundary layers. *Journal of Atmospheric Sciences*, 29(1):91–115, 1972.

[6] James W Deardorff. James W. Deardorff. *Boundary-Layer Meteorol*, 157:343–344, 2015.

[7] Colleen M Kaul, Shreyas Ananthan, MJ Churchfield, Jeff D Mirocha, Larry K Berg, and R Rai. Large-eddy simulations of idealized atmospheric boundary layers using Nalu-Wind. In *Journal of Physics: Conference Series, volume=1452, number=1, pages=012078, year=2020, organization=IOP Publishing.*

[8] Caroline Draxl, Dries Allaerts, Eliot Quon, and Matt Churchfield. Coupling mesoscale budget components to large-eddy simulations for wind-energy applications. *Boundary-Layer Meteorology*, 179(1):73–98, 2021.

[9] William C Skamarock, Joseph B Klemp, Jimy Dudhia, David O Gill, Zhiquan Liu, Judith Berner, Wei Wang, Jordan G Powers, Michael G Duda, Dale M Barker, et al. A description of the advanced research WRF model version 4. *National Center for Atmospheric Research: Boulder, CO, USA*, 145:145, 2019.

[10] Domingo Muñoz-Esparza, Branko Kosović, Jeff Mirocha, and Jeroen van Beeck. Bridging the transition from mesoscale to microscale turbulence in numerical weather prediction models. *Boundary-layer meteorology*, 153(3):409–440, 2014.

[11] D Muñoz-Esparza, B Kosović, J Van Beeck, and J Mirocha. A stochastic perturbation method to generate inflow turbulence in large-eddy simulation models: Application to neutrally stratified atmospheric boundary layers. *Physics of Fluids*, 27(3):035102, 2015.

[12] Jeff Mirocha, Branko Kosović, and Gokhan Kirkil. Resolved turbulence characteristics in large-eddy simulations nested within mesoscale simulations using the Weather Research and Forecasting Model. *Monthly Weather Review*, 142(2):806–831, 2014.

[13] Paul M Markowski and George H Bryan. LES of laminar flow in the PBL: A potential problem for convective storm simulations. *Monthly Weather Review*, 144(5):1841–1850, 2016.

[14] LJ Mazzaro, E Koo, D Muñoz-Esparza, JK Lundquist, and RR Linn. Random force perturbations: A new extension of the cell perturbation method for turbulence generation in multiscale atmospheric boundary layer simulations. *Journal of Advances in Modeling Earth Systems*, 11(7):2311–2329, 2019.

[15] Gavin R Tabor and MH Baba-Ahmadi. Inlet conditions for large eddy simulation: A review. *Computers & Fluids*, 39(4):553–567, 2010.

[16] Frank J Zajaczkowski, Sue Ellen Haupt, and Kerrie J Schmehl. A preliminary study of assimilating numerical weather prediction data into computational fluid dynamics models for wind prediction. *Journal of Wind Engineering and Industrial Aerodynamics*, 99(4):320–329, 2011.

[17] G Usera, ANTON Vernet, and JA Ferré. A parallel block-structured finite volume method for flows in complex geometry with sliding interfaces. *Flow, Turbulence and Combustion*, 81(3):471–495, 2008.

[18] Mariana Mendina, Martin Draper, Gabriel Narancio, Gabriel Usera, and Ana Paula Kelm Soares. A General Purpose Parallel Block Structured Open Source Flow Solver. In *2012 Seventh International Conference on P2P, Parallel, Grid, Cloud and Internet Computing, pages=273–278, year=2012, organization=IEEE.*

[19] Mariana Mendina, Martin Draper, Ana Paula Kelm Soares, Gabriel Narancio, and Gabriel Usera. A general purpose parallel block structured open source incompressible flow solver. *Cluster Computing*, 17(2):231–241, 2014.

[20] Joseph Smagorinsky. General circulation experiments with the primitive equations: I. The basic experiment. *Monthly weather review*, 91(3):99–164, 1963.

[21] Domingo Muñoz-Esparza, Branko Kosović, Clara García-Sánchez, and Jeroen Van Beeck. Nesting turbulence in an offshore convective boundary layer using large-eddy simulations. *Boundary-layer meteorology*, 151(3):453–478, 2014.

[22] Domingo Muñoz-Esparza and Branko Kosović. Generation of inflow turbulence in large-eddy simulations of nonneutral atmospheric boundary layers with the cell perturbation method. *Monthly Weather Review*, 146(6):1889–1909, 2018.

[23] Sue Ellen Haupt, Branko Kosovic, William Shaw, Larry K Berg, Matthew Churchfield, Joel Cline, Caroline Draxl, Brandon Ennis, Eunmo Koo, Rao Kotamarthi, et al. On bridging a modeling scale gap: Mesoscale to microscale coupling for wind energy. *Bulletin of the American Meteorological Society*, 100(12):2533–2550, 2019.

[24] SE Haupt, Larry K Berg, A Decastro, David J Gagne, Pedro Jimenez, Timothy Juliano, Branko Kosovic, Jeff D Mirocha, Eliot Quon, Jeremy Sauer, et al. Report of the Atmosphere to Electrons Mesoscale-to-Microscale Coupling Project (FY2019). Technical report, Pacific Northwest National Lab.(PNNL), Richland, WA (United States . . . , 2019.

[25] Chin-Hoh Moeng and Peter P Sullivan. A comparison of shear-and buoyancy-driven planetary boundary layer flows. *Journal of Atmospheric Sciences*, 51(7):999–1022, 1994.

[26] Bowen Zhou, Jason S Simon, and Fotini K Chow. The convective boundary layer in the terra incognita. *Journal of the Atmospheric Sciences*, 71(7):2545–2563, 2014.

[27] Jakob Mann. Wind field simulation. *Probabilistic engineering mechanics*, 13(4):269–282, 1998.